Research Square

Preprints are preliminary reports that have not undergone peer review.
They should not be considered conclusive, used to inform clinical practice,
or referenced by the media as validated information.

On-orbit observations and optical interpretation of liquid interfaces in a plate-type propellant tank under microgravity

Di Wu
Chinese Academy of Sciences
Jia Wang
wangjia@imech.ac.cn

Chinese Academy of Sciences
Shangtong Chen
Chinese Academy of Sciences
Shuyang Chen
Chinese Academy of Sciences
Chao Yang
Chinese Academy of Sciences
Jianwu He
Chinese Academy of Sciences
Li Duan
Chinese Academy of Sciences
Qi Kang
Chinese Academy of Sciences

Research Article

Keywords: Microgravity, Capillary interface, Propellant management, On-orbit experiment, Optical measurement, Plate-type tank

Posted Date: November 26th, 2026

DOI: https://doi.org/10.21203/rs.3.rs-11804562/v1

License: This work is licensed under a Creative Commons Attribution 4.0 International License.
Read Full License

Additional Declarations: No competing interests reported.

On-orbit observations and optical interpretation of liquid interfaces in a plate-type propellant tank under microgravity

Di Wu[1,2], Jia Wang[1,2,*], Shangtong Chen[1], Shuyang Chen[1], Chao Yang[1,2], Jianwu He[1,2], Li Duan[1,2], and Qi Kang[1,2,*]

1 Institute of Mechanics, Chinese Academy of Sciences, Beijing 100190, China

2 School of Engineering Science, University of Chinese Academy of Sciences, Beijing 100049, China

Corresponding author: Qi Kang; e-mail: kq@imech.ac.cn, Jia Wang; e-mail: wangjia@imech.ac.cn.

Abstract

Liquid-interface observation in flight hardware is challenging under microgravity because wetting structures produce curved interfaces that can obscure the contact line. This study presents on-orbit observations of butane in a plate-type propellant tank aboard the Space Environment Comprehensive Exploration Satellite (SY-01). The tank incorporates an additively manufactured titanium-alloy assembly of flow-directing plates, anti-slosh plates, an accumulator, and a central column. An internal array of fiducial markers enables comparison between images acquired without propellant and images refracted through the liquid interface. Displacements of 270 identifiable markers show radial and azimuthal components, consistent with a concave interface influenced by the internal structures. Numerical equilibrium configurations at liquid volume fractions of 50.00% and 41.67% provide a qualitative comparison with the observed image features. A spherical-bubble geometric-optics model reproduces the general decrease in radial viewing-angle distortion with increasing marker polar angle, but does not reproduce the measured sign change or the magnitude of the peripheral distortion. These discrepancies are consistent with departures from a spherical interface near the central column and anti-slosh plates. The observations support the feasibility of fiducial-marker imaging for identifying interface features in a metal microgravity tank. Quantitative residual-propellant gauging requires calibration, uncertainty analysis, and validation using independent reference measurements.

Keywords: Microgravity; Capillary interface; Propellant management; On-orbit experiment; Optical measurement; Plate-type tank

1 Introduction

Liquid storage and acquisition in microgravity require control of the gas–liquid interface because buoyancy no longer reliably separates the phases or maintains liquid coverage of an outlet. Propellant management devices (PMDs) use capillary forces and wetting structures to establish connected liquid pathways and limit gas ingestion (Behruzi et al. 2007; Hartwig 2016). Liquid motion can also couple to spacecraft dynamics, motivating studies of sloshing and interface stability (Faltinsen and Timokha 2013; Ikeda et al. 2012). For flight tanks, observing the liquid distribution is important both for evaluating fluid management and for developing methods of residual-propellant estimation.

Screen-based and vane- or plate-based PMDs provide different approaches to capillary liquid acquisition. Plate-type flight tanks incorporate flow-directing structures, accumulators, and anti-slosh elements to retain and redistribute liquid (Tam et al. 1996, 1998). Their operation depends on local geometry and wetting. The theory of capillary free surfaces provides a basis for understanding liquid configurations in corners (Concus and Finn 1974), while studies of rounded-corner flow and open capillary channels have examined transport and stability under reduced gravity (Chen et al. 2006; Grah et al. 2008; Rosendahl and Dreyer 2007). Drop-tower and related studies have extended this understanding to rounded corners, oval tubes, varying cross sections, and eccentric annuli (Han et al. 2019; Chen et al. 2021, 2022, 2023a, 2023b).

Space experiments provide access to sustained microgravity conditions that complement ground-based tests. SPHERES-Slosh and FLUIDICS investigated interface motion in transparent tanks (Lapilli et al. 2015; Dalmon et al. 2019), while the Zero-Boil-Off Tank experiment addressed coupled thermal and fluid-management processes (Kassemi et al. 2018). Tianyuan-1 demonstrated space liquid transport and related fluid-management functions (Li et al. 2022). Experiments aboard the Chinese Space Station have examined free-surface profiles, liquid climbing during filling, and bubble configurations in tanks containing a central column (Chen et al. 2024a, 2024b, 2024c, 2024d). These studies establish the importance of internal structures in determining microgravity interfaces.

In a metal flight tank, optical access is restricted and the liquid contact line may lie outside the camera field of view. Refraction through the interface then becomes part of the measurement rather than merely an imaging artifact. An internal marker array offers a way to relate image displacement to interface curvature, although the mapping is affected by non-axisymmetric wetting structures and departures from an idealized interface. The present study examines this approach in a butane tank integrated with a liquefied-gas cold-gas micropropulsion payload.

The payload was flown aboard the Space Environment Comprehensive Exploration Satellite (SY-01). This paper describes the tank and observation arrangement, compares ground-reference and on-orbit images, and interprets marker displacements using numerical interface configurations and a geometric-optics model. The emphasis is on the observable features of a capillary-controlled interface in flight hardware and the limits of

their optical interpretation. Quantitative residual-mass accuracy and continuous feed performance are not established by the image analysis presented here.

2 Experimental apparatus

The cold-gas micropropulsion payload comprises a microthruster cluster and a storage/supply and electronics unit (Fig. 1). The observation system includes a plate-type butane tank, a valve manifold, a gas–liquid separator, tank and tubing cameras, and platinum-resistance temperature sensors. The tank camera records the internal interface indirectly through the appearance of the wetted structures and fiducial markers; the tubing camera observes the transparent section near the tank outlet.

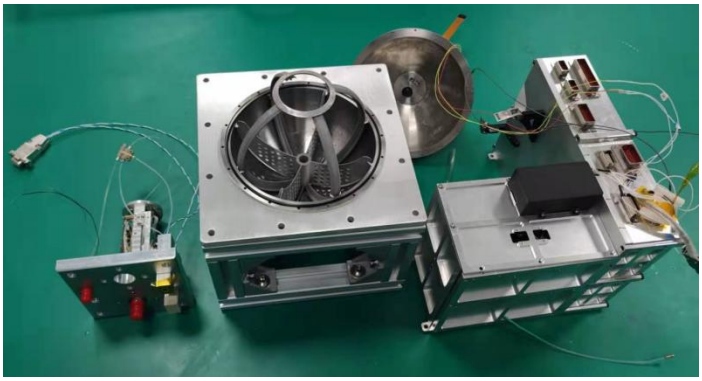

Fig. 1 Photograph of the cold-gas micropropulsion payload and its propellant storage and supply system

Figure 2 shows the storage and supply layout. Capillary structures guide liquid butane toward the tank outlet. The liquid line passes through a valve manifold and a solenoid valve before reaching the gas–liquid separator. The manifold provides filling, isolation, pressure sensing, and overpressure protection. Temperature locations T5–T8 monitor the upper and lower regions of the tank and separator. The tank and manifold are mounted outside the electronics enclosure, and the separator is installed inside it. This arrangement provides the thermal and operational context for the interface observations.

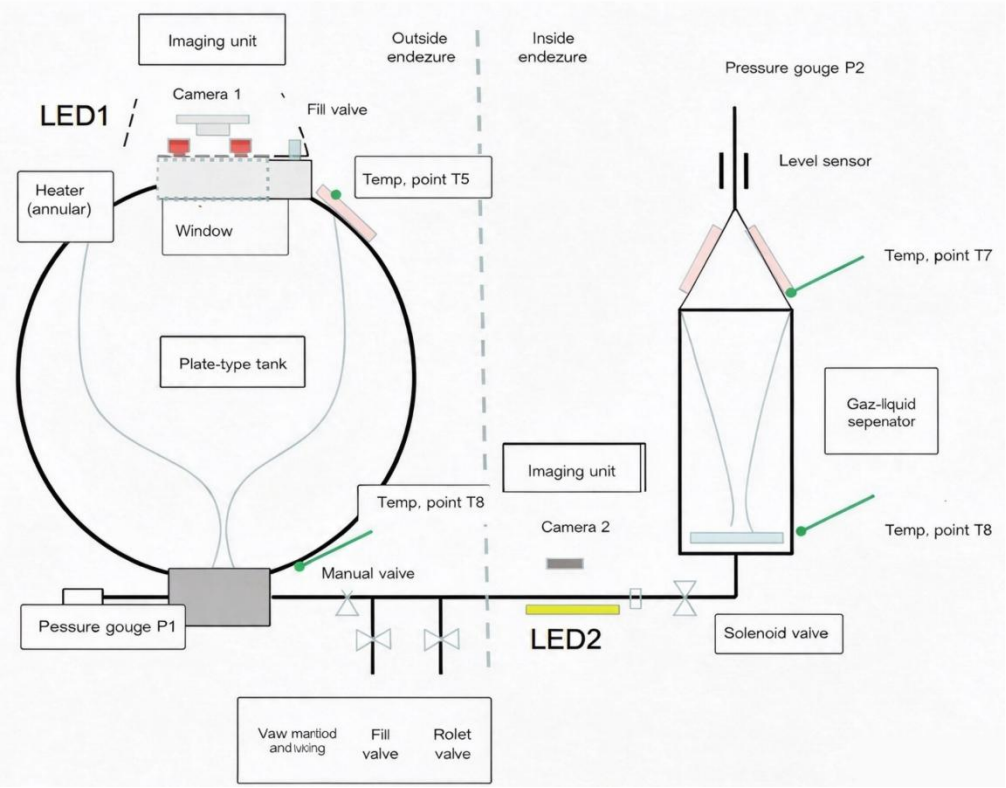

Fig. 2 Schematic of the propellant storage and supply system

2.1 Plate-type tank and internal structures

The titanium-alloy tank has an outside diameter of 150 mm, a wall thickness of 2 mm, a reported internal capacity greater than 1.5 L, and a design pressure above 2 MPa. The development prototype used flanged upper and lower hemispheres; the flight unit used a welded construction. Figure 3 shows the tank and its internal architecture. The tank is supported within a 150 × 160 × 170 mm installation envelope. In this paper, “upper” and “lower” refer to the hardware orientation shown in the schematics; these labels do not imply a gravity-defined vertical direction in orbit.

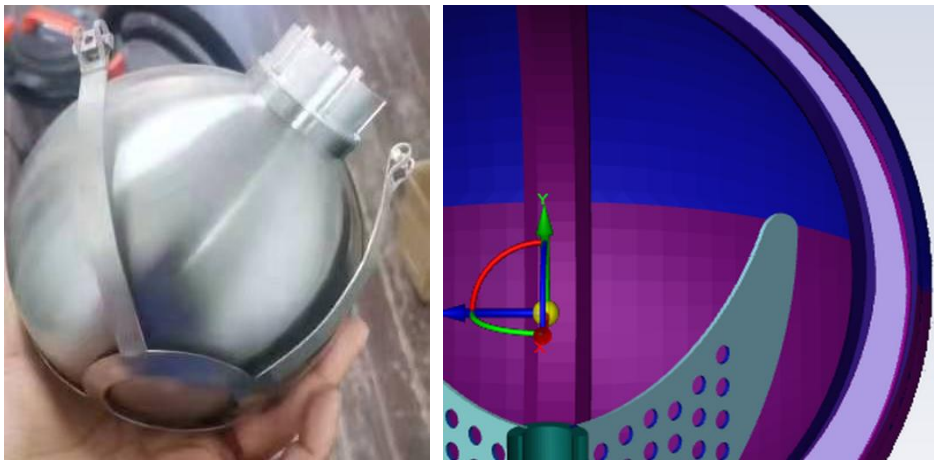

(a) Tank photograph (b) Internal architecture

Fig. 3 Design of the plate-type propellant tank

Four flow-directing channels connect the tank interior to an accumulator near the outlet. The design incorporates T-shaped flow-directing plates and asymmetric gaps between the plates and the shell. An accumulator formed by eight willow-leaf-shaped blades is intended to maintain liquid coverage of the outlet. Four ports in the central column are located below the flow-directing plates, and a conical hole provides a vent path. Four groups of perforated anti-slosh plates partly enclose the outlet region. The central column and plate assembly were additively manufactured as an integrated titanium-alloy component. These structures impose geometric constraints on the interface; their comparative transport or structural performance is outside the scope of the present observations.

A top-mounted camera views the tank through a circular optical window, while light-emitting diodes illuminate the interior through a separate window [Fig. 4(a)]. The stated camera resolution is 640 × 640 pixels. An axisymmetric array of fiducial markers on the tank wall provides a reference for detecting refraction-induced image displacement [Fig. 4(b)]. A wedge-shaped feature and local thermal control were incorporated near the windows to discourage liquid accumulation. In the available on-orbit image, the field of view remained clear enough for marker identification.

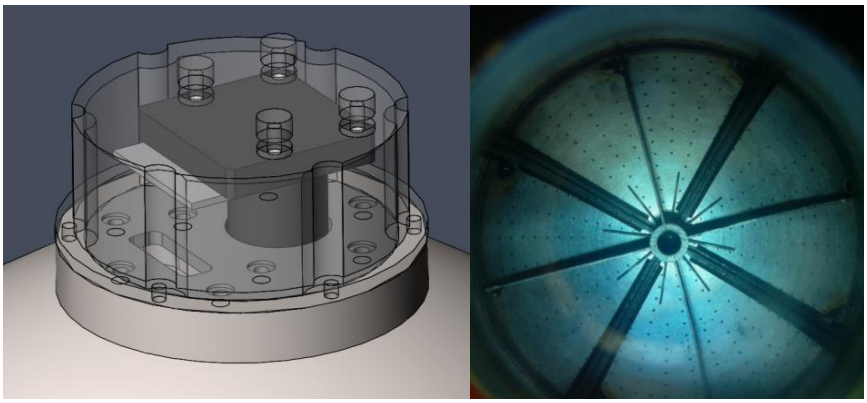

(a) Tank visualization design (b) Tank camera image without propellant

Fig. 4 In-orbit imaging configuration and representative tank image

2.2 Gas–liquid separator and thermal arrangement

The gas–liquid separator provides the downstream thermal and phase-management environment (Fig. 5). Its cylindrical chamber contains a plate-type accumulator in the liquid region and a heater near the gas region, with a wedge separating the two regions. Liquid enters through a lower throttling orifice. A proportional–integral–derivative controller regulates the upper heater, while temperature sensors monitor both ends of the chamber. The intended function is to retain liquid in the accumulator and supply vapor downstream. The present paper reports the associated temperature history but does not quantify gas quality or supply-pressure stability.

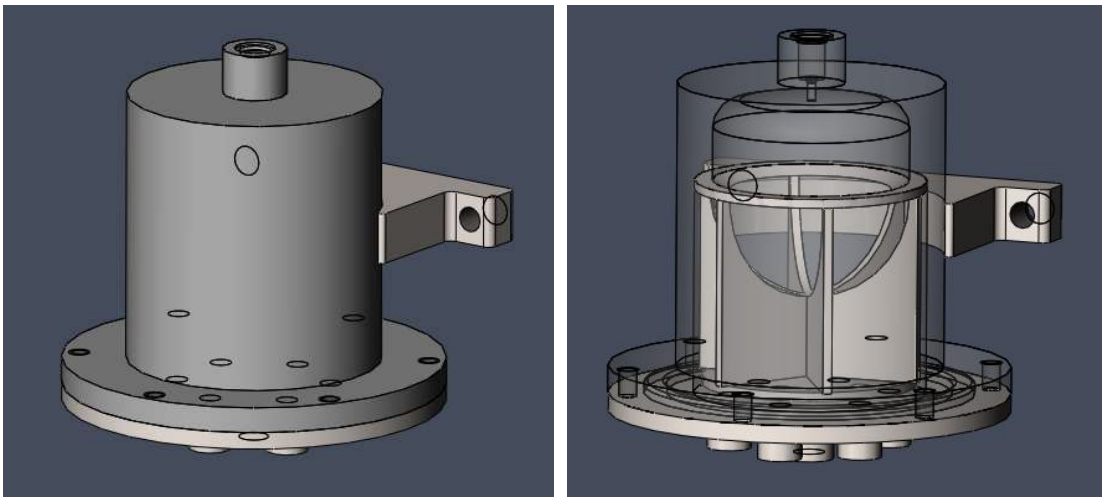

(a) External view (b) Internal configuration

Fig. 5 Gas-liquid separator: (a) external view; (b) internal configuration

2.3 Valve manifold and tubing observation

The valve manifold contains a manual valve, a relief valve, a fill valve, and a pressure sensor (Fig. 6). The manual valve provides ground isolation and is opened before launch. The reported relief-valve opening pressure is 0.8 MPa. A Lee solenoid valve controls the liquid line downstream of the manifold.

A transparent tube of stated diameter 6 mm is installed near the tank outlet for imaging, while 1/16-in. tubing is used elsewhere in the liquid line. A transition fitting contains a 7-μm filter. The observation module combines a close-up lens and an LED diffuser to image the transparent section (Fig. 7). Tubing images can indicate visible gas inclusions at the observation location; identifying their origin also requires the local pressure, temperature, and valve state.

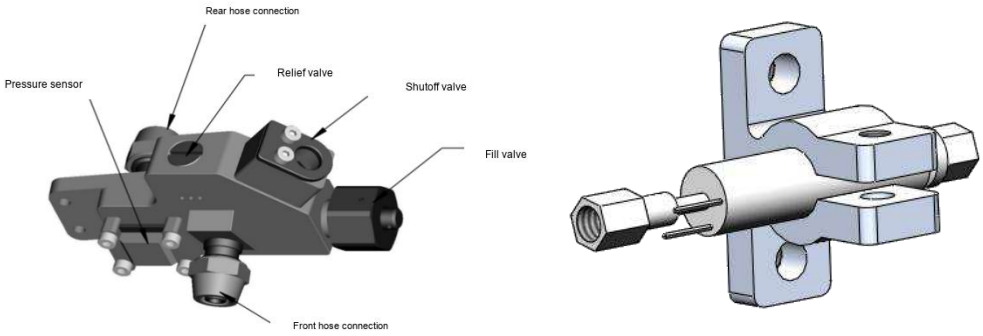

(a) Mechanical valve manifold (b) Lee solenoid valve

Fig. 6 Valve-manifold components

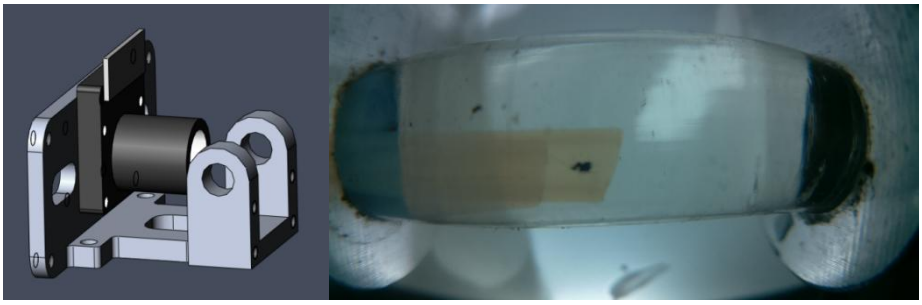

(a) Observation fixture (b) Liquid flow in the transparent tube

Fig. 7 Tubing observation module

3 Experimental procedure and analysis

3.1 On-orbit observation sequence

The observation sequence combined spacecraft thermal control, tank imaging, and tubing imaging. After the payload electronics and tank camera were powered on, the tank-top heater setpoint was specified as 25 °C. The tubing camera was then activated, and the separator-heater setpoint was specified as 30 °C. The cameras and heaters were subsequently switched off. These setpoints describe commanded conditions; the measured temperatures at $T5$–$T8$ are shown in Fig. 8.

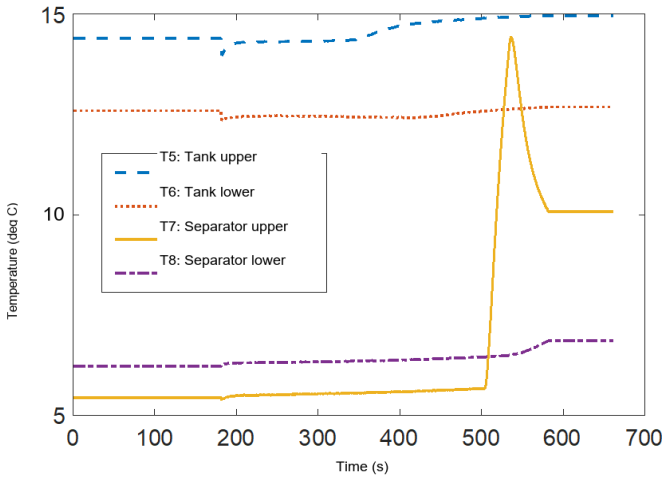

Fig. 8 Measured temperature histories at the upper and lower regions of the tank ($T5$, $T6$) and separator ($T7$, $T8$) during the observation sequence

3.2 Fiducial-marker analysis

Marker positions in the on-orbit image were compared with those in the no-propellant reference image. A total of 270 identifiable markers were used. Displacement was resolved into radial and azimuthal components relative to the image center. Radial viewing-angle distortions were grouped by marker polar angle and averaged to obtain the mean trend. The markers constitute spatial samples of the observed interface and are not independent repetitions of the flight experiment.

3.3 Numerical and optical comparisons

Static numerical interface configurations were obtained for liquid volume fractions of 50.00% and 41.67%. They are compared qualitatively with the observed image features. A separate spherical-bubble geometric-optics model is used to examine the radial trend in marker displacement. Because the optical model does not include the full non-axisymmetric interface, it is treated as an interpretive approximation rather than a calibrated inverse method for liquid-volume estimation.

4 Results and discussion

4.1 Ground-reference images and nominal inventory

The tank was filled with butane on 17 March 2022, with a loaded mass of 0.437 kg. A butane detector indicated 0 ppm during the checks after filling and 24 h later; this means that no butane was detected under those measurement conditions. Ground images acquired on 22 and 24 May 2022 show the interface after a 90° change in tank orientation (Fig. 9). The image-based liquid-volume estimate was 0.6750 L, corresponding to a mass estimate of 0.405 kg. The difference from the loaded mass is 0.032 kg. Liquid stored in the tubing and other supply components can contribute to this difference, but a component-wise mass balance and

measurement uncertainties are needed before this comparison can establish gauging accuracy or quantify leakage.

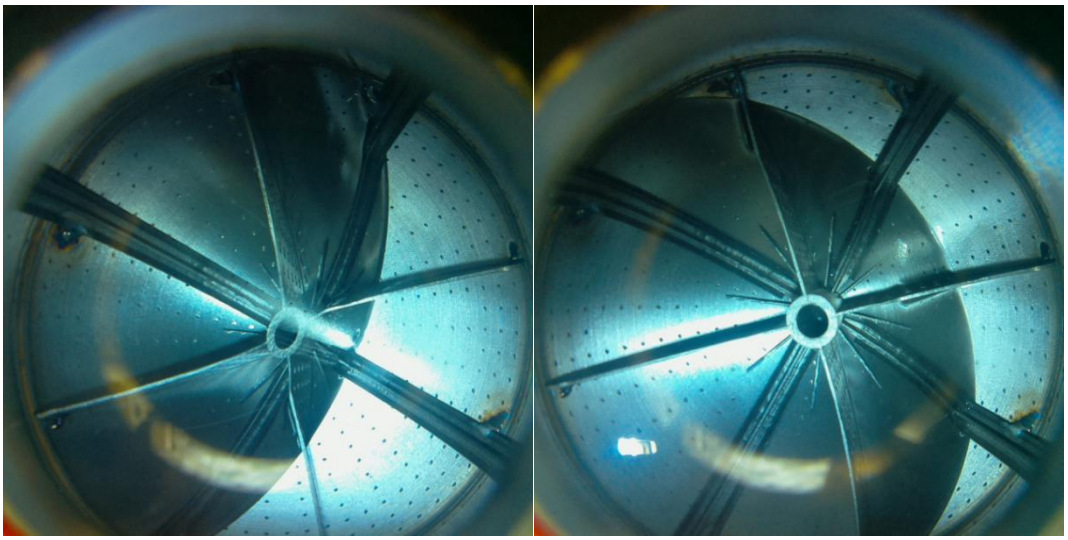

(a) 22 May 2022 (b) 24 May 2022

Fig. 9 Integrated satellite test after butane loading

4.2 On-orbit interface features

After launch and orbital insertion, the tank camera recorded a clear view of the internal structures [Fig. 10(a)]. Unlike the ground images in Fig. 9, the on-orbit image does not show a readily identifiable contact line. The optical interpretation is that the lower hemisphere is viewed through a curved gas–liquid interface, with portions of the contact line outside the field of view. A concave refracting interface can reduce the apparent image size and expand the visible region, consistent with the appearance of three markers on the upper hemisphere. Four bright regions occur near the flow-directing plates, indicating an azimuthally structured optical response.

Figure 10(b) compares reference marker locations (red) with their on-orbit locations (green). The displacement contains both radial and azimuthal components. An ideal centered, axisymmetric spherical interface would produce only a radial displacement field in the corresponding aligned optical geometry. The observed azimuthal component is therefore consistent with a non-axisymmetric interface influenced by the plates. Local displacement near the anti-slosh structures and the reflected or refracted illumination features are also consistent with liquid climbing along these structures. This interpretation requires accurate image registration and optical calibration to distinguish interface effects from camera misalignment and lens distortion.

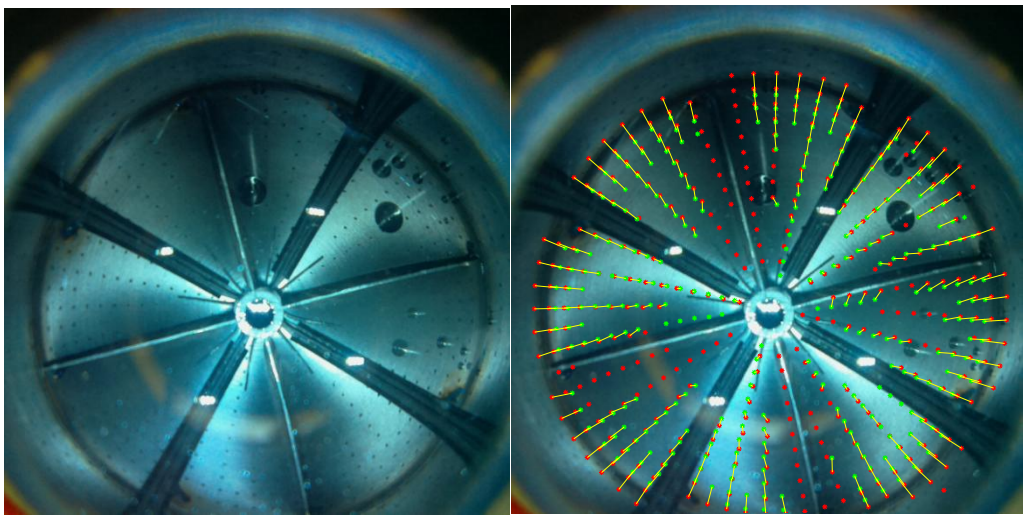

(a) Tank image (b) Fiducial-marker displacement

Fig. 10 On-orbit tank images and fiducial-marker displacement

4.3 Comparison with numerical interface configurations

The numerical configurations in Fig. 11 illustrate the effect of liquid volume fraction. At 50.00%, the interface is closer to a spherical configuration and extends upward along the flow-directing plates. At 41.67%, the interface contacts the upper region of the anti-slosh plates and exhibits greater curvature. The latter configuration is consistent with the qualitative interpretation of the on-orbit image. In this comparison, the ground-estimated volume of 0.6750 L is associated with the nominal 41.67% condition. Quantitative comparison requires a consistent effective-volume definition and confirmation of the liquid inventory at the time of flight imaging. The available images do not provide a direct three-dimensional reconstruction of the interface.

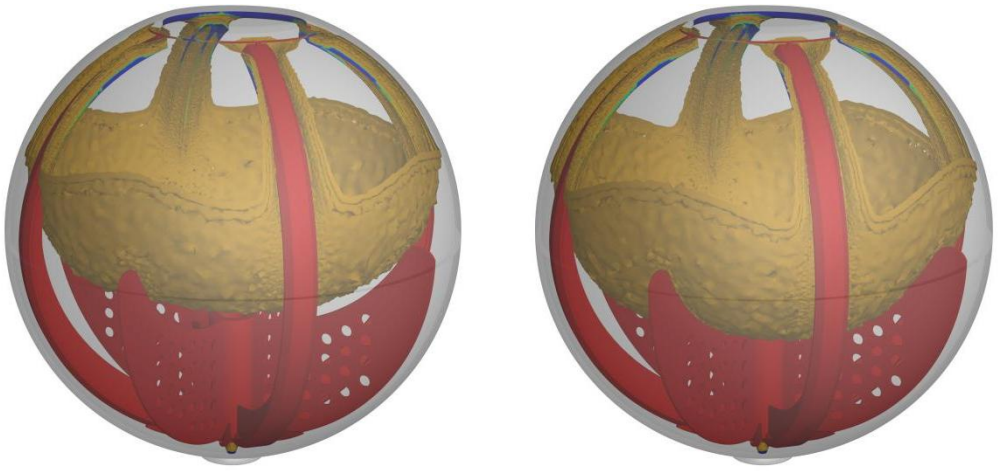

(a) Liquid volume fraction 50.00% (b) Liquid volume fraction 41.67%

Fig. 11 Numerically predicted equilibrium interface at two liquid volume fractions

4.4 Geometric-optics interpretation

The simplified optical construction is shown in Fig. 12(a). A spherical gas bubble of radius r has its center O_2 displaced by h from the tank center O_1. A marker P lies on the spherical tank wall of radius R at polar angle θ. In the idealized geometry, the camera pupil C is located at the upper pole, and the marker viewing angle without liquid is $\theta/2$. A ray connecting P and C crosses the interface at A. With the gas refractive index approximated as unity and the liquid refractive index denoted by n, optical reversibility gives the Snell relation in Eq. (1).

$$\sin\varphi = n \sin\varphi' \qquad (1)$$

Here $\varphi = \angle CAO_2$ denotes the gas-side angle and $\varphi' = \angle PAB$ the liquid-side angle with the interface normal, following the ray construction in Fig. 12(a). The viewing-angle shift is $\Delta\alpha$, and $d = AC$. Angular relations follow the convention shown in Fig. 12(a).

Applying the sine rule to triangle CAO_2 gives

$$\frac{r}{\sin(\theta/2 - \Delta\alpha)} = \frac{R - h}{\sin\varphi} = -\frac{d}{\sin(\theta/2 - \Delta\alpha + \varphi)} \qquad (2)$$

where the center-to-pupil distance is $CO_2 = R - h$.

Applying the sine rule to triangle PAC gives

$$\frac{2R\cos(\theta/2)}{\sin(180° - \varphi + \varphi')} = \frac{d}{\sin[360° - (180° - \varphi + \varphi') - \Delta\alpha]} \qquad (3)$$

Defining $\Delta\varphi = \varphi - \varphi'$ gives the nonlinear system

$$\begin{cases} \sin\varphi - n\sin(\varphi - \Delta\varphi) = 0 \\ r\sin\varphi - (R - h)\sin(\theta/2 - \Delta\alpha) = 0 \\ (R - h)\sin(\theta/2 - \Delta\alpha + \varphi) + d\sin\varphi = 0 \\ 2R\cos(\theta/2)\sin(\Delta\varphi - \Delta\alpha) - d\sin(\Delta\varphi) = 0 \end{cases} \qquad (4)$$

For specified geometry and refractive index, the system is solved for φ, $\Delta\varphi$, d, and $\Delta\alpha$. The resulting Δα represents the change in apparent viewing angle of a marker at polar angle θ. The spherical-interface assumption excludes local menisci around the central column and the anti-slosh plates.

Figure 12(b) shows example rays for $r/R = 0.74$ and the stated liquid volume fraction of 40.5%. Markers are equally spaced in arc length to represent the physical array. Rays near the center are deflected less than those near the periphery, explaining the general increase in distortion magnitude with polar angle. This illustrative optical case is distinct from the 41.67% numerical configuration and should not be interpreted as an independently fitted flight inventory.

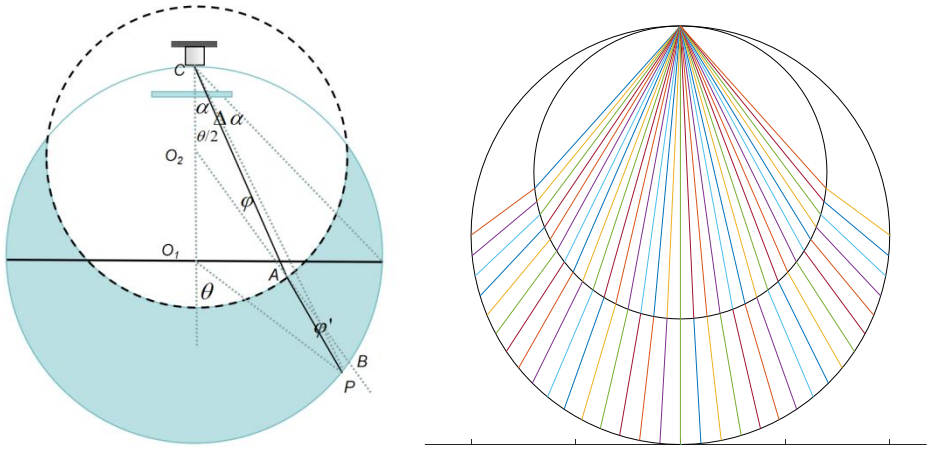

(a) Camera-imaging geometry (b) Rays entering the camera pupil at a 40.5% liquid volume fraction

Fig. 12 Geometric-optics model for fiducial-marker imaging

Figure 13(a) compares the measured marker distortions and their grouped means with the spherical-bubble prediction. Both show a decreasing radial viewing-angle distortion as the marker polar angle increases. However, the measured mean changes sign near 22.5°, whereas the model gives zero distortion at the center and negative values away from it. The model also underestimates the magnitude of the negative peripheral distortion. These systematic differences limit the model to qualitative interpretation. A non-spherical interface that rises along the central column can alter the local surface normal and produce opposite displacement signs in the inner and outer regions, as sketched in Fig. 13(b). This mechanism is consistent with the observed pattern, but quantitative attribution requires optical prediction using the actual three-dimensional interface.

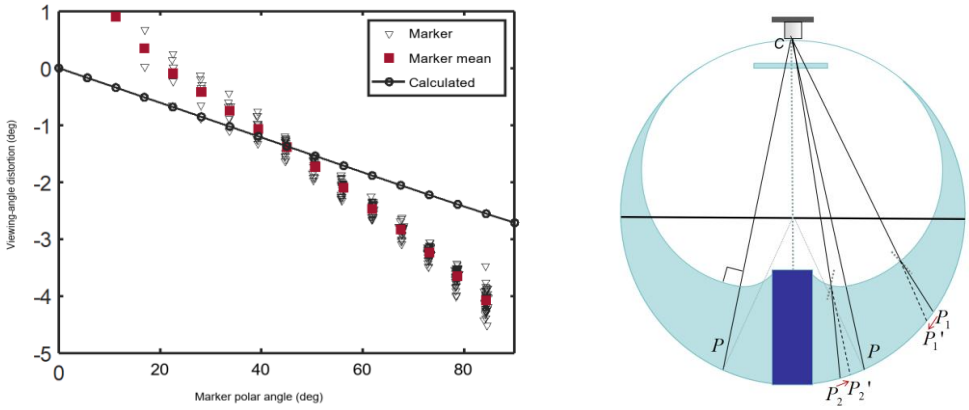

(a) Measured and model-predicted marker distortion (b) Interpretation of the positive and negative image shifts

Fig. 13 Radial viewing-angle distortion and its interpretation: (a) individual markers, grouped means, and the spherical-bubble prediction; (b) schematic showing how a non-spherical interface can produce image shifts of opposite sign

4.5 Implications and limitations

The flight observations show that internal markers remain identifiable in a metal tank containing a capillary-managed liquid. Their displacement field contains information about interface shape even when the contact line is not directly visible. The azimuthal component and the departure from the spherical prediction indicate that the internal structures must be included when interpreting the images. These findings motivate a combined interface-shape and optical model for future measurements.

The present evidence is limited to the documented imaging conditions and qualitative comparisons. A single-view displacement field does not by itself establish a unique three-dimensional interface or an accurate residual mass. Lens and window refraction, image registration, wetting conditions, thermal gradients, and residual acceleration must be characterized to quantify uncertainty. The reported temperature differences also mean that isothermal equilibrium should be treated as a modeling assumption requiring assessment rather than an experimentally demonstrated condition.

The image interpretation is consistent with liquid occupying the outlet region and climbing along the internal structures. It does not quantify continuous feed duration, gas ingestion, downstream vapor quality, or pressure stability. Establishing those engineering characteristics requires synchronized operating-state records and independent flow or pressure measurements. Likewise, extending the optical method to residual-propellant gauging requires calibration over known liquid inventories and validation under representative microgravity interface conditions.

5 Conclusions

On-orbit images of a plate-type butane tank were analyzed using an internal fiducial-marker array. The displacement of 270 identifiable markers contains radial and azimuthal components consistent with a concave, non-axisymmetric interface influenced by the flow-directing plates, anti-slosh structures, and central column. Numerical configurations at 50.00% and 41.67% liquid volume fractions provide qualitative support for this interpretation. A spherical-bubble optical model explains the overall radial trend but does not reproduce the measured sign change or peripheral distortion. The results demonstrate the feasibility of obtaining interface-sensitive optical information in a metal microgravity tank. Further calibration and a model incorporating the actual interface are required before quantitative residual-propellant accuracy can be established.

Statements and Declarations

Acknowledgments: This work was supported by the China Manned Space Engineering Program(KJZ-YY-NLT0603) and the National Natural Science Foundation of China (Grant Nos. 12102438, 12032020, and 12072354).

References

Behruzi, P., Dodd, C., Netter, G.: Future Propellant Management Device Concepts for Restartable Cryogenic Upper Stages. In: 43rd AIAA/ASME/SAE/ASEE Joint Propulsion Conference & Exhibit (2007). https://doi.org/10.2514/6.2007-5498

Chen, S., Ye, Z., Duan, L., Kang, Q.: Capillary driven flow in oval tubes under microgravity. Physics of Fluids 33, 032111 (2021). https://doi.org/10.1063/5.0040993

Chen, S., Wu, D., Li, Y., Liu, J., Duan, L., Li, W.: Profiles of Liquid on the Surface of Revolution with Varying Cross-section under Microgravity. Microgravity Science and Technology 34, 106 (2022). https://doi.org/10.1007/s12217-022-10024-x

Chen, S., Wu, D., Li, W., Ding, F., Kang, Q., Li, Y.: Capillary Phenomena in Tubes Under Microgravity. Brazilian Journal of Physics 53, 135 (2023a). https://doi.org/10.1007/s13538-023-01328-3

Chen, S., Guo, L., Li, Y., Liu, J., Kang, Q., Li, W.: Capillary-driven flows in eccentric annuli under microgravity. Archive of Applied Mechanics 93, 731-743 (2023b). https://doi.org/10.1007/s00419-022-02295-y

Chen, S., Hu, L., Chen, S., Zhang, P., Chen, Y., Chen, Z., Liu, X., Zhao, X., Wu, D., Wang, J., Ye, Z., Duan, L., Yin, Y., Kang, Q.: Study on the shape and motion of bubbles in the tank model with a central column aboard the Chinese Space Station. Physics of Fluids 36, 012124 (2024a). https://doi.org/10.1063/5.0180681

Chen, S., Duan, L., Li, W., Chen, S., Kang, Q.: Profiles of free Surfaces in Revolved Containers Under Microgravity. Microgravity Science and Technology 36, 11 (2024b). https://doi.org/10.1007/s12217-023-10093-6

Chen, S., Chen, S., Wu, D., Duan, L., Liu, X., Zhao, X., Zha, P., Yang, C., Hu, L., Wang, J., Zhao, Y., Yin, Y., Kang, Q.: Study on Liquid Climbing Behavior During Filling Process in Tank Models Aboard the Chinese Space Station. Microgravity Science and Technology 36, 36 (2024c). https://doi.org/10.1007/s12217-024-10123-x

Chen, Y., Weislogel, M.M., Nardin, C.L.: Capillary-driven flows along rounded interior corners. Journal of Fluid Mechanics 566, 235-271 (2006). https://doi.org/10.1017/s0022112006001996

Chen, Z., Duan, L., Chen, S., Li, C., Yang, C., Hu, L., Zhang, P., Wu, D., Zhang, Y., Pang, H., Zhao, Y., Kang, Q.: Study of Morphology of Gas–Liquid Interfaces in Tank with Central Column in CSS under Different Gravity Conditions. Symmetry 16, 878 (2024d). https://doi.org/10.3390/sym16070878

Concus, P., Finn, R.: On capillary free surfaces in the absence of gravity. Acta Mathematica 132, 177-198 (1974). https://doi.org/10.1007/bf02392113

Dalmon, A., Lepilliez, M., Tanguy, S., Alis, R., Popescu, E.R., Roumiguié, R., Miquel, T., Busset, B., Bavestrello, H., Mignot, J.: Comparison Between the FLUIDICS Experiment and Direct Numerical Simulations of Fluid Sloshing in Spherical Tanks Under Microgravity Conditions. Microgravity Science and Technology 31, 123-138 (2019). https://doi.org/10.1007/s12217-019-9675-4

Faltinsen, O.M., Timokha, A.N.: Multimodal analysis of weakly nonlinear sloshing in a spherical tank. Journal of Fluid Mechanics 719, 129-164 (2013). https://doi.org/10.1017/jfm.2012.635

Grah, A., Haake, D., Rosendahl, U., Klatte, J., Dreyer, M.E.: Stability limits of unsteady open capillary channel flow. Journal of Fluid Mechanics 600, 271-289 (2008). https://doi.org/10.1017/s0022112008000529

Han, Z., Duan, L., Kang, Q.: Behavior of a liquid drop in a rounded corner: Different contact angles. AIP Advances 9, 085203 (2019). https://doi.org/10.1063/1.5100300

Hartwig, J.W.: A Detailed Historical Review of Propellant Management Devices for Low Gravity Propellant Acquisition. In: 52nd AIAA/SAE/ASEE Joint Propulsion Conference (2016). https://doi.org/10.2514/6.2016-4772

Ikeda, T., Ibrahim, R.A., Harata, Y., Kuriyama, T.: Nonlinear liquid sloshing in a square tank subjected to obliquely horizontal excitation. Journal of Fluid Mechanics 700, 304-328 (2012). https://doi.org/10.1017/jfm.2012.133

Kassemi, M., Kartuzova, O., Hylton, S.: Results of the microgravity Zero-Boil-Off Tank (ZBOT) experiment. in Proceedings of the 69th International Astronautical Congress (2018), Paper IAC-18-A2.6.43028

Lapilli, G., Kirk, D.R., Gutierrez, H., et al.: Results of microgravity fluid dynamics captured with the SPHERES-Slosh experiment. in Proceedings of the International Astronautical Congress (2015)

Li, G., Huang, Y., Han, W., Wu, Z., Yang, Y.: Space Liquid Transport Experiments in Tianyuan-1. Microgravity Science and Technology 34, 100 (2022). https://doi.org/10.1007/s12217-022-10004-1

Rosendahl, U., Dreyer, M.E.: Design and performance of an experiment for the investigation of open capillary channel flows. Experiments in Fluids 42, 683-696 (2007). https://doi.org/10.1007/s00348-007-0274-6

Tam, W., Lay, W., Hersh, M., Jaekle, Jr., D., Epstein, S.: Design, development, qualification, and manufacture of the HS 601 propellant tank. In: 32nd Joint Propulsion Conference and Exhibit (1996). https://doi.org/10.2514/6.1996-2748

Tam, W., Jaekle, Jr., D., Farokhi, S.: Design and manufacture of the HS 601 Block II propellant tank assembly. In: 34th AIAA/ASME/SAE/ASEE Joint Propulsion Conference and Exhibit (1998). https://doi.org/10.2514/6.1998-3199